Experimental Quiescent Drifting Dusty Plasmas and Temporal Dust Acoustic Wave Growth

J. R. Heinrich,[1] S. -H. Kim,[1] J. K. Meyer,[1] and R. L. Merlino[1]

Department of Physics and Astronomy, The University of Iowa, Iowa City, Iowa, 52242, USA

(Dated: 19 September 2011)

We report on dust acoustic wave growth rate measurements taken in a dc (anode glow) discharge plasma device. By introducing a mesh with a variable bias $12 - 17$ cm from the anode we developed a technique to produce a drifting dusty plasma. A secondary dust cloud, free of dust acoustic waves, was trapped adjacent to the anode side of the mesh. When the mesh was returned to its floating potential the secondary cloud was released and streamed towards the anode and primary dust cloud, spontaneously exciting dust acoustic waves. The amplitude growth of the excited dust acoustic waves was measured directly along with the wavelength and Doppler shifted frequency. These measurements were compared to fluid and kinetic dust acoustic wave theories. As the wave growth saturated a transition from linear to nonlinear waves was observed. The merging of the secondary and primary dust clouds was also observed.

I. INTRODUCTION

Dusty plasmas are four component plasmas made up of ions, electrons, neutral gas atoms and charged sub-micron to micron sized dust grains. Typically these dust grains are large enough to scatter visible light and have a plasma frequency low enough to allow for visual investigation. Dusty plasmas support a variety of plasma waves including the dust acoustic wave (DAW), a density wave that propagates through the charged dust suspension,[1] first observed in 1995.[2] Dust acoustic wave growth occurs when the free energy source, typically a net ion-flow with respect to the dust grains in laboratory dusty plasmas, is large enough to overcome the inherent damping found in dusty plasma suspension, which can be due to inter-grain correlation, dust-neutral collisions, etc.[3] The growth rate of a wave is computed from its dispersion relation, which details the dependence of the wave frequency and growth rate on the wavenumber. The DAW dispersion relation has been derived using both fluid theory[4–6] and kinetic theory[7–9] to various degrees of complexity.

Experimental investigation of the real part of the DAW dispersion relation has been conducted by numerous groups.[10–15] In these experiments, DAWs were driven by a low frequency oscillating current modulated through a range of frequencies. The resulting wave numbers were measured, and the wave numbers and frequencies were constructed into a wave-spectrum that could be compared to theoretical dispersion relations. These frequency synchronization experiments dealt directly with the real part of the dispersion relation and did not investigate the imaginary part, the growth rate. The growth rate has been experimentally measured through various techniques.[13,16,17] In these experiments spatial DAW growth was measured in dust clouds already experiencing dust density fluctuations from previously excited DAWs. Recently, by transitioning a plasma from an over-damped to an underdamped dusty plasma suspension for DAWs, DAW growth was observed at the onset of the DAW instability by Flanagan and Goree.[18] Here, in an rf discharge device with dust confined into a three dimensional cloud, Flanagan and Goree excited and measured the growth of DAWs as the neutral pressure (dust-neutral collision rate) was reduced, verifying damping of DAWs by dust-neutral collisions in the process. As the neutral damping was further reduced, Flanagan and Goree were able to observe the development of nonlinearity in DAWs.[19] In their experiment the DAWs were strongly damped (with neutral argon gas pressures above 400 mTorr), the dust experienced strong coupling effects, and the spatial

growth rates were measured in a dust suspension that supported about 3 wavelengths.

Previous experiments investigating fundamental DAW phenomena have used external potentials to manipulate dusty plasmas.[20,21] When a probe (object) is introduced into a dusty plasma it develops a sheath and the probe's electric potential creates a dust void.[22,23] In the present work, in which a similar induced potential was created with a biased mesh, we developed a technique to trap and release a secondary dust cloud, far from the primary dust cloud in a moderately coupled dc discharge plasma. When released, the secondary dust cloud drifted toward the anode, and DAWs appeared when the cloud was a certain distance from the anode. A linear growth phase followed by wave amplitude saturation was observed. The measured growth rates of the excited waves were compared with fluid and kinetic models. The new experimental technique of forming a drifting dusty plasmas allowed us to follow the growth of DAWs from nearly thermal fluctuations. Also, this technique allowed us to perform temporal growth measurements of weakly damped DAWs in a moderately coupled quiescent dusty plasma of sufficient size to support many wavelengths.

II. EXPERIMENTAL DESIGN AND METHODS

The experiment was conducted in an anodic discharge apparatus 90 cm in length by 60 cm in diameter, shown in Fig. 1(a). A plasma was established under a 5 - 7 mA (300 V) discharge current between the 3.2 cm diameter anode and the vacuum chamber wall with a 4 mT axial magnetic field (for electron confinement) and an argon gas pressure of 150 mTorr (20 Pa). An axial discharge electric field of $\sim$ 200 V/m, measured with an emissive probe in the absence of dust, produced a net ion-flow. Dust particles, located below the anode on an electrically floating tray, became charged, lifted, and incorporated into the anode glow. The experiment was repeated for two species of dust, spherical iron and monodisperse spherical silica powder. The iron dust had a size range of $r_d \approx 0.5$ - 5 μm and the silica dust had a radius of $r_d \approx 0.5$ μm. Once a sufficiently dense dust cloud ($n_d \sim 1 \times 10^{10}$ m^{-3}) was collected, a circular mesh (12 cm in diameter) was moved into the plasma, 14 to 15 cm from the anode, shown in Fig. 1(a). The mesh had an inter-wire space of 0.87 mm. Once the mesh was in place, a -50 V bias was applied between the mesh and the chamber wall, creating a non-monotonic electric field. The bias produced a plasma glow around the mesh and the resulting potential configuration trapped dust grains, creating a secondary

dust cloud adjacent to the anode side of the mesh, shown in Fig. 1(b). The axial electric potential profiles of the experimental apparatus with a biased mesh and a floating mesh are shown in Fig. 2. The positive potential well created by the biased mesh is not as deep as the potential well created by the anode. Consequentially, dust trapped in the secondary cloud can be expected to be colder than dust trapped in the primary cloud. The topology and density of the secondary cloud was controlled by adjusting the anode discharge current, the potential applied to the mesh, and the distance between the mesh and the anode. When the bias was released from the mesh (i.e. the mesh was allowed to return to its floating potential), the electric field became monotonic again at ≈ 210 V/m (in the region where the dust drifted) and the secondary dust cloud drifted to the positively biased anode. Dust acoustic waves spontaneously appeared in the drifting dust cloud. By increasing the distance between the anode and the mesh the streaming dust 'channel' could be transformed from a large/wide 'channel' to a narrow 'channel' or jet. For longer distances the dust had larger drift velocities, well above the dust acoustic phase velocity, C_{da}, with Mach numbers (with respect to the primary dust cloud) above 2.

The dust particles were illuminated with a 2 mm wide 532 nm laser sheet at 300 mW and the dust dynamics were recorded using a lens filter, to eliminate background light, at 250 frames per second with a Photron (FASTCAM 1024 PCI) CMOS camera, which has a linear response to light intensity. The image sizes were 1024 by 1024 pixels, giving pixel resolution between 1.8 and 2.2 mm/pixel. The laser light scattered by the mesh was subtracted from each frame. Image slices parallel to $\mathbf{k}$ (the direction of wave propagation, in this case $\mathbf{z}$) were taken from the captured frames and converted into an intensity array, (z_j,I_{zj}), where z_j is the distance from the anode and I_{zj} is the corresponding image intensity in frame number j. The established coordinate system is shown in Fig. 1(b) (x is parallel to the laser sheet). The camera's linear response to light intensity allows for pixel intensities to be transformed into dust densities, $\mathrm{I} \propto n_d$, so that the intensity arrays could be converted into arrays of normalized dust density N_d, $N_d = (I - I_{ave})/I_{ave} = (n_d - n_{d0})/n_{d0}$. Once the images were formatted, a tracking routine was used to obtain the bulk motion of the secondary dust cloud and the wave speed and amplitude of the spontaneously excited DAWs. While individual particle tracking in the described experiment is impossible due to the pixel resolution constraints, an average dust velocity was obtained by tracking the mean streaming dust cloud position.

The plasma density and electron temperature were measured in the absence of dust (probes disturb dusty plasmas[22]) with a double Langmuir probe axially from the anode. In the region where DAW growth was observed n_i ranged from $\approx (2-4) \times 10^{13}$ m^{-3} with an electron temperature $T_e \approx 2.5$ eV. The ion temperature is estimated as the neutral gas temperature, $T_i \approx T_n \approx 0.025$ eV. The experiment with iron particles was conducted with a 7 mA discharge and the experiment with silica dust was conducted with a 5 mA discharge. With both iron and silica particles DAW growth was observed in regions with similar plasma density, the difference in discharge current was offset by the difference in distance from the anode. The axial plasma density profiles for the 5 mA and 7 mA discharge currents are shown in Fig. 3.

Dust particles may be heated by thermal electric field fluctuations in the background plasma and via DAWs driven by an ion-flow instability.[24–26] We expect dust trapped in the potential well of the mesh to have a much lower kinetic energy than dust trapped in the primary cloud near the anode due to the weaker confining potential and the absence of DAWs (i.e. an ion-flow). The absence of DAWs leaves only thermal electric field fluctuations as a potential heating source. From a thermodynamics calculation, Avinash *et al.* estimate a dust temperature in a quiescent dusty plasma of $T_d \approx (1 + Z_d^2 n_d/2n_i)T_i$,[26] giving the streaming dust a temperature $\sim 5 - 10$ eV. For our theoretical comparison we take $T_d = 5$ eV.

Dust densities in complex plasmas, particularly in strongly coupled suspensions, are typically obtained directly from the inter-particle spacing. The current experiment does not allow for direct measurement of the inter-particle spacing. Another technique, that does not require resolving individual particles, involves measuring the extinction of light through the dust cloud, the amount of light scattered and absorbed by the dust suspension.[27,28] The later method is also insufficient as it calculates the average density for the region the light is passed through and cannot be easily applied in our experimental apparatus. To obtain a dust density in our apparatus we employed a combination of these methods.

To calculate the dust density in some region of the dust cloud the total pixel intensity over that portion is measured and summed, I_{tot}. The selected region's total pixel intensity is compared with the total pixel intensity of light scattered by a single particle; the pixel intensity from a single particle is simply measured when dust particles can be individually identified, often possible in less dense dust cloud regions. Taking the total pixel intensity

scattered from a single particle, I_p, the total number of dust particles illuminated can be approximated, $n_d \times volume = I_{tot}/I_p$. Using the volume of the region (the illuminated cloud width is the laser sheet width, 2 mm), the dust density is easily calculated. The observed streaming dust had densities $n_d \approx (2-5) \times 10^9$ m^{-3}. When individual dust grains cannot be isolated, pixel intensities can still be used to obtain the relative dust densities between different portions of the dust suspension as well as N_d. Similar techniques to obtain dust density have been used before.[17]

III. OBSERVATIONS AND RESULTS

While the mesh was biased, the secondary cloud was stationary, stable, and free of DAWs. When the bias voltage was removed, and the mesh was floating, the secondary dust cloud began drifting toward the anode. Once the secondary dust cloud travelled a certain distance from the mesh, DAWs became excited. Images of the drifting cloud and the excitation of DAWs along with the corresponding dust density profiles are shown in Fig. 4. Since the dust cloud was drifting, the DAWs were Doppler shifted with respect to the lab-frame. Relative to the dust frame, a Doppler frequency shift is measured by the moving (lab) receiver. The ions drift away from the anode (DAWs naturally propagate along the ion flow direction, as they do in the primary cloud) while the secondary cloud drifts towards the anode. Evidence for a Doppler shift can been seen in the wavefront and dust density profiles; in the lab-frame there is a curvature of the wavefronts opposite to the direction of propagation, Fig. 4(c), as well as a steepening of the wave's trailing edge. Both of these traits are indicative of semi-planar DAWs propagating in the opposite direction, showing that the DAWs are strongly Doppler shifted. To better examine the drifting dust cloud, the one dimensional spatial path of the secondary cloud to the anode and the resulting DAWs was plotted in a space-time diagram. Sample space-time diagrams taken from typical experimental runs are shown in Fig. 5(a) and (b). The following description of a typical experimental run corresponds to the space-time diagram in Fig. 5(a). Initially, the dust cloud begins to expand and accelerate towards the anode from $t \approx 0$ to 0.3 s. At $t \approx 0.3$ s the dust cloud has reached its terminal velocity. At $t \approx 0.5$ s DAWs first appeared. As the drifting dust cloud approaches the anode it slows (along with the lab-frame phase speed of the drifting DAWs) until the drifting DAWs propagate with the primary DAWs, seen in Fig. 5(a) at $t \sim 1$ s at a distance of $z \sim 5$ cm.

Once the secondary dust cloud stopped streaming, the primary dust cloud grew in size and density. Wave-wave interactions between the drifting and primary DAWs were observed. The nature of the wave-wave interactions depended on the drift speed of the secondary cloud. Lower drift speeds resulted in the smooth transition from drifting DAWs to non-drifting DAWs, seen in Fig. 5(a) from $t \approx 0.9$ to 2 s. Larger drift speeds resulted in wave-wave collisions between the drifting and non-drifting DAWs, seen in Fig. 5(b) from $t \approx 0.5$ to 1.4 s. More details of the wave-wave interactions will be provided in a subsequent paper.

As the drifting DAWs were excited their density perturbations were seen growing in time. Converting slices of the video frames into averaged density arrays (z_j, N_{dzj}), plotted in Fig. 6(b), the amplitudes for the growing waves, ΔN_d, were measured from trough to peak through time. From these amplitude evolutions the growth rate was measured directly by fitting an exponential of the form $\Delta N_d = A_t \exp(\omega_i * t)$ (where A_t and ω_i are the fitting parameters) to the temporal amplitude growth. Parameter A_t takes into account the initial amplitude as well as the time difference between the initial wave growth and when measurements were taken. Examples of the observed amplitude growth along with the growth rate fittings are shown in Fig. 6(a) and (c). When silica dust was used, the observed growth rates fell between 20 to 30 s^{-1} with an average of 26 ± 4 s^{-1}. For iron dust the observed growth rates fell between 10 to 20 s^{-1} with an average of 17 ± 3 s^{-1}. The exponential fits used to calculate the growth rates typically had correlation coefficients, R, greater than .98.

The waves exhibited linear growth until the wave amplitudes began to saturate and nonlinear wave steepening was observed. The linear to nonlinear transition of the growing waves can be seen in the wave profiles of Fig. 6(b), between 0.10 and 0.16 s, and of Fig. 6(d), between 0.06 and 0.09 s, where the waves profiles steepen from sinusoidal to non-sinusoidal wave amplitudes. Nonlinear waves were observed after the growth rate saturated.

The inertial streaming DAW frequency depends on the DAW drift velocity. The average secondary dust cloud velocity, u_{ds}, was used for the DAW drift velocity. This approximation was found to be self-consistent by comparing DAW speeds before and after the secondary dust cloud slowed and merged completely with the primary cloud (as $u_{ds} \to 0$, $C_{da(lab)} = u_{ds} + C_{da} \to C_{da}$, where C_{da} is the DA speed in the dust frame). The method proved valuable since the lab-frame dust acoustic speed, for both the drifting and non-drifting waves, and the average secondary dust cloud velocity were easily observable. With the streaming drift velocity, the dust-frame frequency can be calculated, $f_{lab} = f_{dust}(u_{ds} + C_{da})/C_{da}$ (note:

$\lambda_{lab} = \lambda_{dust} = \lambda$). The lab-frame frequency, wavelength, and wave speed were measured directly from the wave profiles and averaged over single experimental runs. The experimental values and uncertainties along with the inertial-frame frequencies are given in Tables I and II for the iron and silica dusts, respectively. The frequencies and velocities are taken with respect to the z-direction.

IV. COMPARISON WITH THEORY

There are three proposed free energy sources for DAWs that are relevant to the observed wave growth. While DAWs are typically excited by an ion-drift with respect to the dust particles in laboratory dusty plasmas, D'Angelo[29] and Shukla *et al.*[30] suggested two additional potential sources of free energy, both related to the acceleration of dust particles by gravity. During the short period of our experiment when the dust acceleration and dust velocity is the greatest there are no visible DAWs present. D'Angelo's model requires a threshold velocity of the dust particles for DAW excitation[29] and does not fit the experimental observations as DAWs are not observed when the streaming dust velocity is maximal (Fig. 5(a) at $t = 0.2$ s, $z = 11$ cm). A similar argument applies to the Shukla *et al.* model[30] as the free energy source. There was no DAW growth until the dust cloud is within some minimum distance of the anode, where the ion-flow is stronger, as expected if the free energy source is from an ion-dust streaming instability. If the free energy source was due to accelerating dust grains the observed wave growth would be expected to occur sooner. Additionally since DAWs were completely absent in the trapped secondary cloud, we assume there was an insufficient ion-flow at large distances from the anode to excite DAWs.

The experimentally measured growth rates were compared with theoretical values taken from both fluid and kinetic models. The models chosen include a static electric field, collisions with neutrals, and finite dust temperature. For the fluid model Merlino provided a dispersion relation[3] that has been used for comparison to experiments under similar conditions.[3,31] The ions, electrons, and dust particles were treated as fluids with the continuity and momentum equations and closed with Poisson's equation:

$$\frac{\partial n_j}{\partial t} + \frac{\partial n_j u_j}{\partial x} = 0, \tag{1}$$

$$n_j m_j \left(\frac{\partial u_j}{\partial t} + u_j \frac{\partial u_j}{\partial x} \right) + \kappa_B T_j \frac{\partial n_j}{\partial x} - q_j n_j E = -\nu_{jn} n_j m_j u_j, \tag{2}$$

and

$$\frac{\partial E}{\partial x} = \frac{e}{\epsilon_0}(n_i - n_e - Z_d n_d). \tag{3}$$

Here j is taken over the three components, the ions, electrons and dust. These equations account for collisions with neutrals, electron and ion inertia, as well as a zeroth order drifts, which accounts for the background electric field, $u_{j0} \propto E_0$. Linearizing and solving Eqs. 1 - 3, assuming all first-order quantities vary as $e^{i(kx-\omega t)}$, yields the dispersion relation:[3]

$$1 - \sum_j \frac{\omega_{pj}^2}{\alpha_j} = 0, \tag{4}$$

where

$$\alpha_j = \Omega_j(\Omega_j + i\nu_{jn}) - k^2 V_{jT}^2. \tag{5}$$

Here $\Omega_j = \omega - k u_{j0}$, $V_{jT} = \sqrt{\kappa_B T_j / m_j}$, and $\nu_{in(en)} = n_n \sigma_{in(en)} V_{iT(eT)}$. The dust-neutral collision frequency was taken from Liu *et al.*,[32] $\nu_{dn} = \delta 8\sqrt{2\pi} m_n n_n r_d^2 V_{nT}/3m_d$ with $\delta = 1.26$. The ion-mobility and ion drift velocity were taken from Robertson *et al.*[33] The electron drift velocity was taken as $u_{e0} = q_e E_0/m_e\nu_{en}$ and the dust drift velocity is taken from the experimental data.

The kinetic model used for comparison is a modified version of models derived by Rosenberg *et al.*[14] and Rosenberg.[34] Rosenberg *et al.*'s model included finite dust temperature, collisions, and drifting Maxwellians for ions and electrons and has previously been used for comparison of DAWs in a similar experimental setup.[14] Briefly, starting with the linear dispersion relation:

$$1 + \sum_j \chi_j = 1 + \sum_j \frac{[1 + \zeta_j Z(\zeta_j)]}{(k^2\lambda_{Dj}^2)\left[1 + (i\nu_{jn}\sqrt{2}kV_{jT})Z(\zeta_j)\right]} = 0, \tag{6}$$

where $\zeta_j = (\omega - k u_{j0} + i\nu_{jn})/\sqrt{2}kV_{jT}$ and $Z(\zeta)$ is the plasma dispersion function, Rosenberg *et al.*[14] simplified Eq. (6) for the long wavelength regime where $u_{e0} \ll V_{et}$, $k u_{i0} > \nu_{in} \gg \omega$, $\omega > kV_{dT}$, $\zeta_e \ll 1$, $2 \geq \zeta_i \gtrsim 1$, and $\nu_{dn} \ll \omega$. Since we expect $\nu_{dn} \approx \omega$ the last approximation is not valid. Instead, we take the dust susceptibility, χ_d, from early work by Rosenberg[34] for DAWs in collisional dusty plasmas where $\zeta_d \gg 1$, which is a reasonable approximation for our experiment for $\lambda \gtrsim 2$ mm with $T_d < 10$ eV. The resulting dispersion relation is:

$$1 + \frac{1}{k^2\lambda_{De}^2} - \frac{\omega_{pi}^2}{k^2 u_{i0}^2 + \nu_{in}^2}$$

$$-i\left(\frac{1}{k^2\lambda_{Di}^2}\sqrt{\frac{\pi}{2}}\frac{u_{i0}}{V_{iT}}\exp\left(-\frac{u_{i0}^2}{2V_{iT}^2}\right)\right)$$
$$-\frac{\omega_{pd}^2}{A_d}=0, \tag{7}$$

where

$$A_d \approx \omega(\omega+i\nu_{dn})-\frac{i\nu_{dn}k^2V_{dT}^2}{\omega+i\nu_{dn}}. \tag{8}$$

The calculated fluid and kinetic dispersion relations are plotted with the experimental observations for iron and silica in Fig. 7 and 8, respectively, for both the real frequencies and growth rates along with experimental uncertainties. For the calculations the following parameters were used: $n_i = 2\times10^{13}$ m^{-3}, $T_d = 5$ eV, $r_d = 0.5$ μm, $n_d = 3\times10^9$, further detailed in Table III. For the case of the iron dust, the range of dust radii may significantly change the modeled dispersion relation. The models predict values for both the real frequencies and growth rates that agree well with the measured values.

V. CONCLUSION

By introducing a mesh cathode that could be switched on and off, we were able to trap and release a secondary dust cloud. When released, the secondary cloud streamed towards the anode and primary cloud, exciting DAWs when within a certain distance of the anode where free energy in the ion-flow is sufficient These streaming waves were Doppler shifted. Temporal DAW growth was observed and the growth rates were measured in a quiescent dust cloud large enough to support many wavelengths. The growth rates of DAWs in silica dust and iron dust were measured and compared to kinetic and fluid theories. The dispersion relations derived from both the fluid and kinetic models predicted real frequencies corresponding to maximum growth that agreed well with the observed frequencies. Growth rates obtained from the kinetic theory were in better agreement with the measured growth rates as compared to those obtained from the fluid theory.

REFERENCES

[1]N. N. Rao, P. K. Shukla, and M. Y. Yu, Planetary and Space Science **38**, 543 (1990).

[2]A. Barkan, R. Merlino, and N. D'Angelo, Physics of Plasmas **2**, 3563 (1995).

[3]R. Merlino, Physics of Plasmas **16**, 124501 (2009).

[4]F. Melandsø and P. K. Shukla, Planetary and Space Science **43**, 635 (1995).

[5]N. D'Angelo, Physics of Plasmas **4**, 3422 (1997).

[6]S. A. Khrapak, A. V. Ivlev, V. V. Yaroshenko, and G. E. Morfill, Phys. Rev. Lett. **102**, 245004 (Jun 2009).

[7]M. Rosenberg, Planetary and Space Science **41**, 229 (1993).

[8]M. Rosenberg, Journal of Vacuum Science and Technology A **14**, 631 (1996).

[9]V. N. Tsytovich and U. de Angelis, Physics of Plasmas **6**, 1093 (1999).

[10]J. B. Pieper and J. Goree, Phys. Rev. Lett. **77**, 3137 (1996).

[11]E. Thomas, R. Fisher, and R. L. Merlino, Physics of Plasmas **14**, 123701 (2007).

[12]C. Thompson, A. Barkan, N. D'Angelo, and R. L. Merlino, Physics of Plasmas **4**, 2331 (1997).

[13]T. Trottenberg, D. Block, and A. Piel, Physics of Plasmas **13**, 042105 (2006).

[14]M. Rosenberg, E. Thomas, and R. L. Merlino, Physics of Plasmas **15**, 073701 (2008).

[15]V. Nosenko, S. K. Zhdanov, S.-H. Kim, J. Heinrich, R. L. Merlino, and G. E. Morfill, EPL **88**, 65001 (2009).

[16]E. Thomas, Physics of Plasmas **13**, 042107 (2006).

[17]V. E. Fortov, A. D. Usachev, A. V. Zobnin, V. I. Molotkov, and O. F. Petrov, Physics of Plasmas **10**, 1199 (2003).

[18]T. M. Flanagan and J. Goree, Physics of Plasmas **17**, 123702 (2010).

[19]T. M. Flanagan and J. Goree, Physics of Plasmas **18**, 013705 (2011).

[20]S. H. Kim, J. R. Heinrich, and R. L. Merlino, Physics of Plasmas **15**, 9 (2008).

[21]J. Heinrich, S.-H. Kim, and R. Merlino, Physical Review Letters **103**, 115002 (2009).

[22]C. O. Thompson, N. D'Angelo, and R. L. Merlino, Physics of Plasmas **6**, 1421 (1999).

[23]E. Thomas, K. Avinash, and R. L. Merlino, Physics of Plasmas **11**, 1770 (2004).

[24]J. Williams and E. Thomas, Physics of Plasmas **14**, 063702 (2007).

[25]G. Joyce, M. Lampe, and G. Ganguli, Physical Review Letters **88**, 9 (2002).

[26]K. Avinash, R. Merlino, and P. Shukla, Physics Letters A **375**, 2854 (2011).

[27]C. F. Bohren and D. R. Huffman, *Absorption and Scattering of Light by Small Particles* (Wiley-Interscience, 1983).

[28]Y. Nakamura and H. Bailung, Review of Scientific Instruments **70**, 2345 (1999).

[29]N. D'Angelo, Physics Letters A **304**, 102 (2002).

[30]P. K. Shukla, M. Salimullah, and G. E. Morfill, Physica Scripta **67**, 354 (2003).

[31]E. Thomas, Physics of Plasmas **17**, 043701 (2010).

[32]B. Liu, J. Goree, V. Nosenko, and L. Boufendi, Physics of Plasmas **10**, 9 (2003).

[33]S. Robertson and Z. Sternovsky, Physical Review E **67**, 046405 (2003).

[34]M. Rosenberg, Journal of Plasma Physics **67**, 04 (2002).

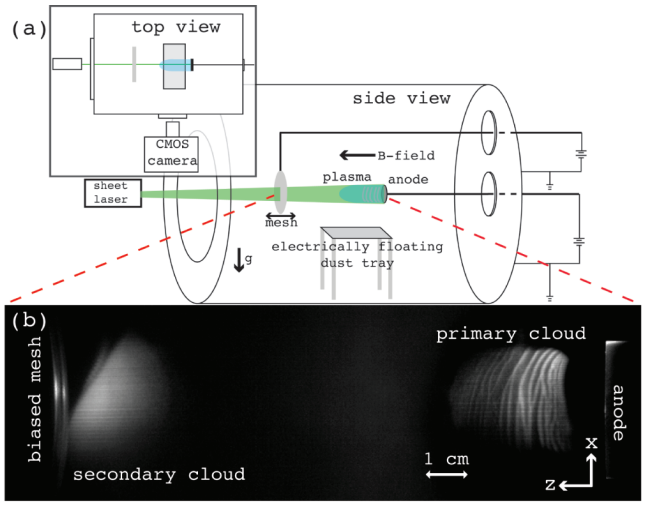

FIG. 1. (color online) (a) Schematics of the experimental apparatus with a 12 cm diameter mesh. The inter-wire spacing of the mesh allowed laser light to pass through unobstructed. The mesh was designed with a variable bias with respect to the chamber, permitting for a secondary dust cloud to be trapped and later ejected when the bias was removed. The distance between the mesh and the anode is adjustable. (b) Image of the dusty plasma suspension with the biased mesh and a trapped secondary dust cloud. The primary and secondary clouds as well the anode, mesh, and coordinate system are labeled. Here the mesh is ~ 15.5 cm from the anode.

TABLE I. Experimental Observations: iron dust

Parameter	Value*	Method/Expression
Measured		
f_{lab}	-11 ± 1.5 Hz	Image analysis
λ	2.7 ± 0.2 mm	Image analysis
u_{ds}	-6.1 ± 0.2 cm/s	Image analysis
$C_{da(lab)}$	-2.9 ± 0.3 cm/s	Image analysis
ω_i	17 ± 3 s^{-1}	Image analysis
Computed		
f_{dust}	12 ± 5 Hz	$f_{lab}C_{da}/(u_{ds}+C_{da})$
C_{da}	3.2 ± 0.4 cm/s	$C_{da(lab)} - u_{ds}$

*Taken in the z-direction

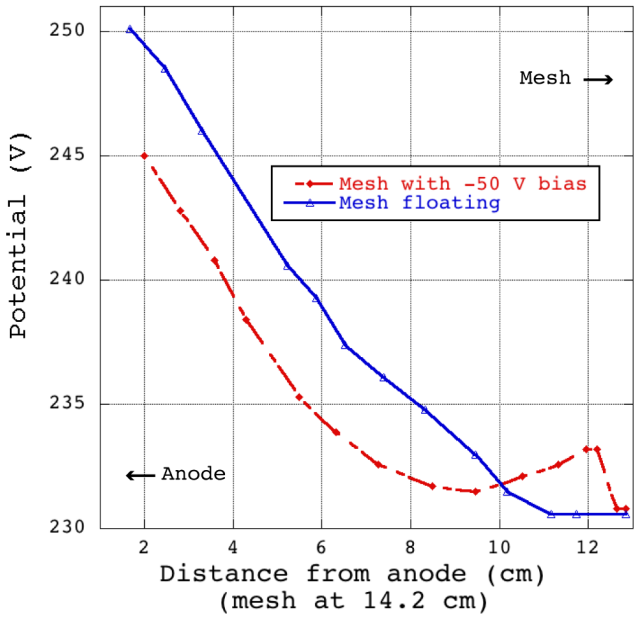

FIG. 2. (color online) Floating potential taken with an emissive probe in the absence of dust. The mesh was located 14.2 cm from the anode. The potential well created by the biased mesh that traps the secondary dust cloud is located from 9 to 13 cm from the anode.

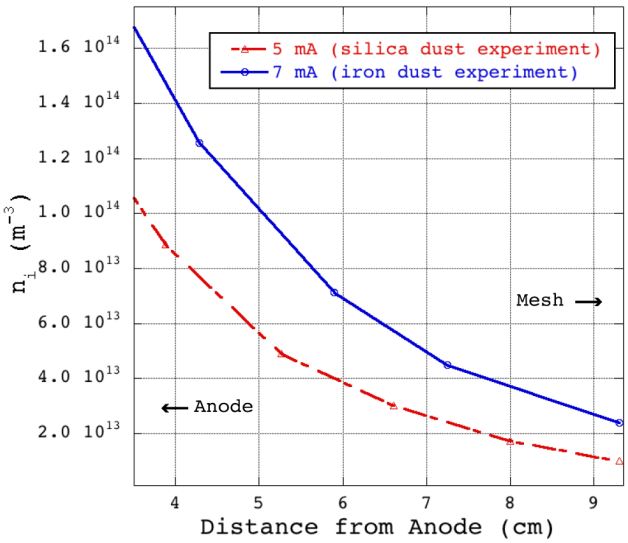

FIG. 3. (color online) Axial plasma density in the absence of dust for 5 and 7 mA discharge currents, corresponding to the silica and iron dust experiments, respectively. The plasma density falls off exponentially from the anode.

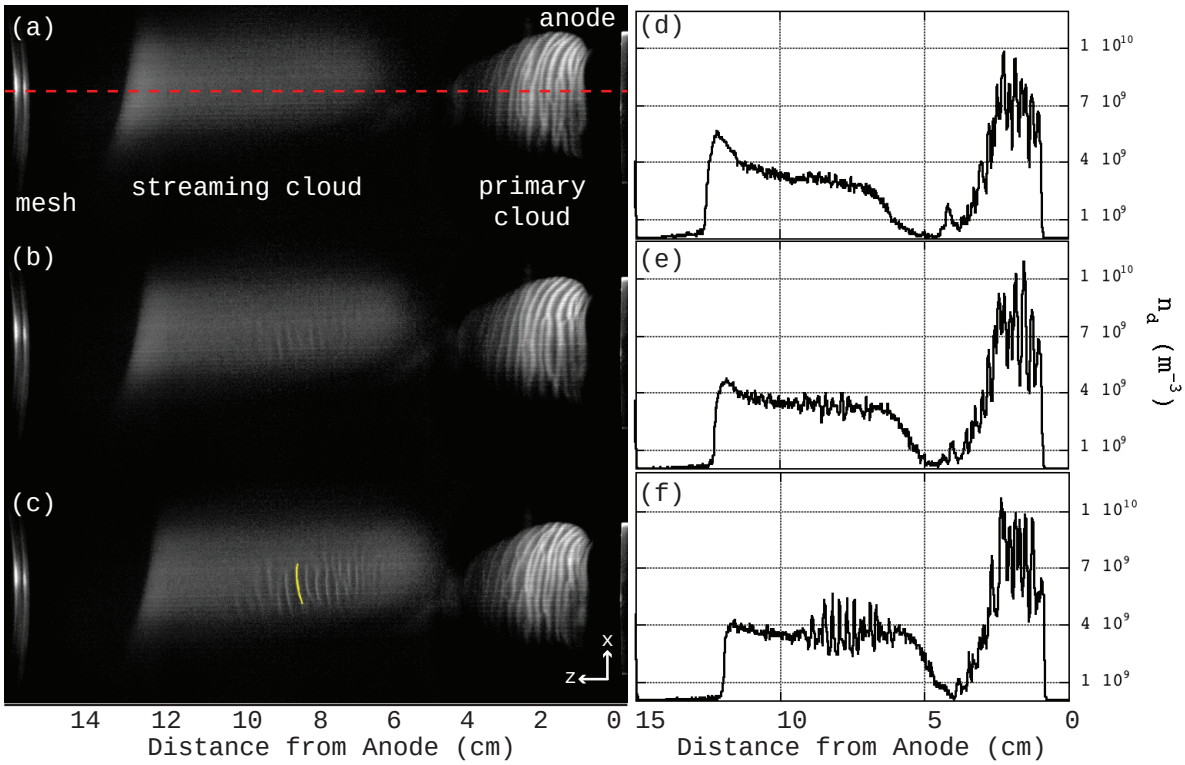

FIG. 4. (color online) Images of the drifting dust cloud with spontaneously excited dust acoustic waves taken at 0.08 second intervals. Taking $\Delta t = 0$ s from the first observable traces of dust acoustic waves, the streaming dust cloud is shown in (a) at $\Delta t = -0.05$ s. Early dust acoustic wave growth is shown in (b) at $\Delta t = 0.03$ s. Fully developed dust acoustic waves are shown in (c) at $\Delta t = 0.11$ s. A curvature in the wavefronts of the streaming dust acoustic waves can be seen in (c) with a sample wavefront highlighted in yellow. (d)-(f) show the corresponding dust density profiles taken across the dotted line in (a). The spatial slice in (a) is also the line that the space-time plot in Fig. 5(a) was taken over. Taken with iron dust.

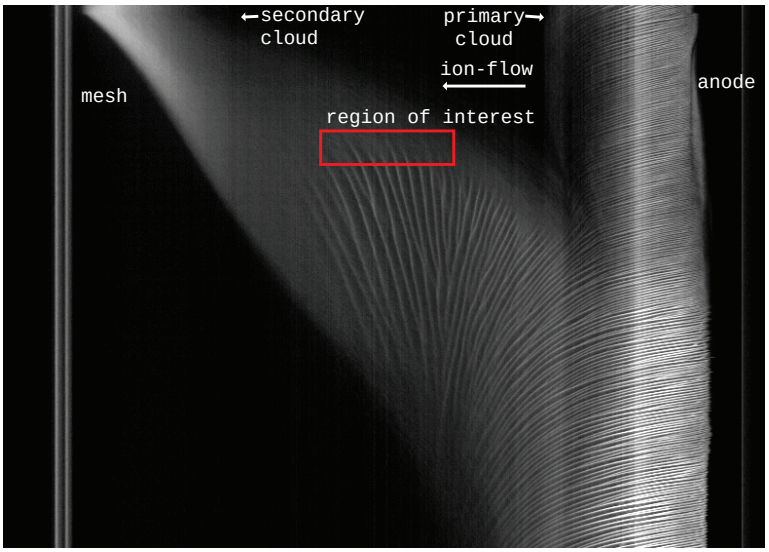

FIG. 5. (color online) Space-time diagram of the spontaneous excitation of dust acoustic waves in a streaming dust cloud. The primary dust cloud is towards the right and the secondary dust cloud is seen towards the top left of the image (note the absence of waves). The anode is the line on the right of the image and the circular mesh is on the left. The region of wave growth is marked and the direction of ion-flow is indicated. The time is taken from when the bias was removed from the mesh. The spatial slice the space-time plot in (a) was taken over is indicated in Fig. 4(a). Average dust cloud drift speeds for (a) and (b) from 0 to 0.5 s are 6.1 and 9.8 cm/s, respectively. The smooth transition between drifting DAWs and non-drifting DAWs seen in (a) from 0.9 to 2 s is due to lower dust drift speed. The wave collisions seen in (b) from 0.5 to 1.4 s are due to a larger dust drift speed. Taken with iron dust.

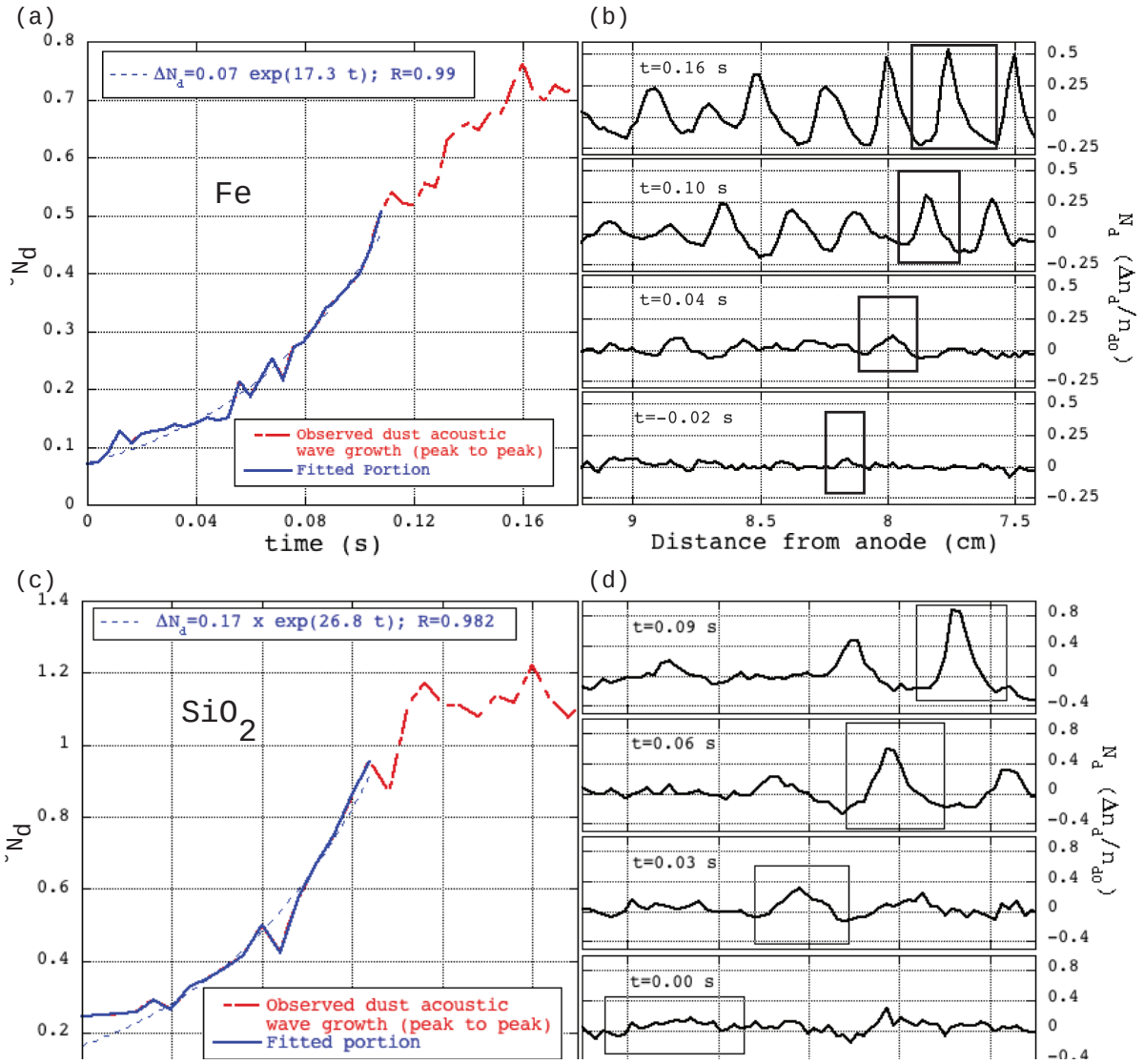

FIG. 6. (color online) Examples of the observed dust acoustic wave growth. In (a),(c) the amplitude measured between the peak and trough of single dust acoustic waves (boxed in (b) and (d)) are plotted vs. time with iron and silica dust, respectively. The portions of the observed amplitude growth used to calculate the growth rate are indicated and the exponential fits used to calculate the growth rates are given. Dust density profiles of several waves are shown in (b), (d), with time taken with respect to (a) and (c). The dust acoustic waves showed linear growth until the waves saturated at around $t \sim 0.16$ s in (b) and $t \sim 0.08s$ in (d). Data in (a) and (b) corresponds to the experimental run shown in Fig. 4 and 5(a).

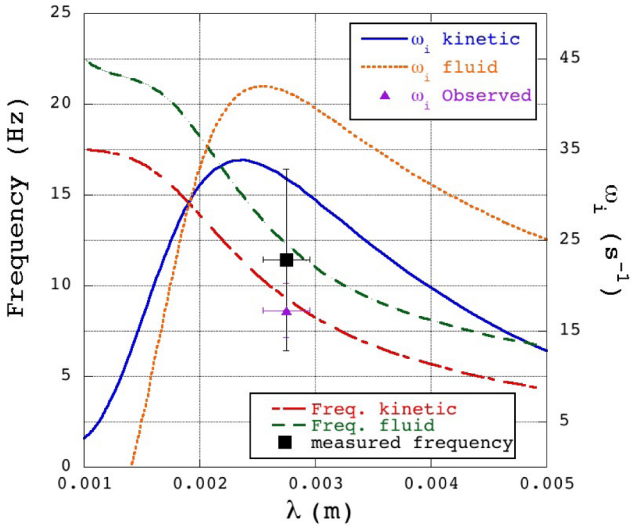

FIG. 7. (color online) Theoretical and observed frequencies and growth rates plotted vs wavelength for iron dust. The observed growth rate and frequency are shown with experimental uncertainty. Theoretical values are plotted for the detailed experimental parameters.

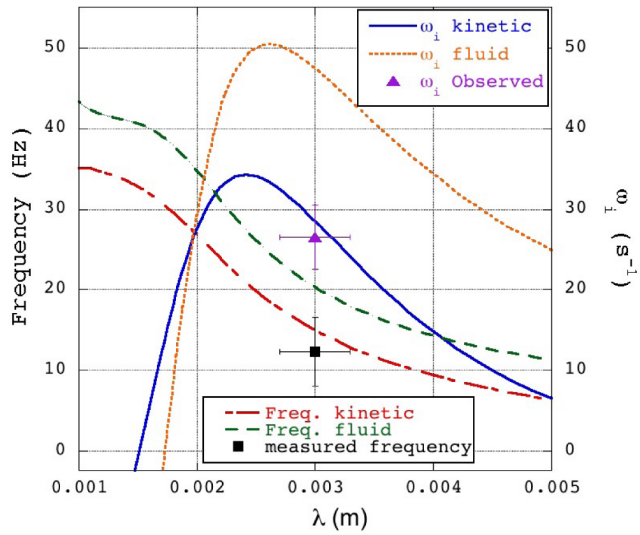

FIG. 8. Theoretical and observed frequencies and growth rates plotted vs wavelength for silica dust. The observed growth rate and frequency are shown with experimental uncertainty. Theoretical values are plotted for the detailed experimental parameters.

TABLE II. Experimental Observations: silica dust

Parameter	Value*	Method/Expression
Measured		
f_{lab}	-24 ± 4 Hz	Image analysis
λ	3.0 ± 0.3 mm	Image analysis
u_{ds}	-10.8 ± 0.3 cm/s	Image analysis
$C_{da(lab)}$	-7.1 ± 0.4 cm/s	Image analysis
ω_i	27 ± 4 s^{-1}	Image analysis
Computed		
f_{dust}	12 ± 4.3 Hz	$f_{lab}C_{da}/(u_{ds} + C_{da})$
C_{da}	3.7 ± 0.3 cm/s	$C_{da(lab)} - u_{ds}$

*Taken in the z-direction

TABLE III. Parameters

Parameter	Value	Expression	Remark
Measured			
n_i	$(2-4)\times 10^{13}$ m^{-3}		Double probe (no dust), axial density shown Fig. 3
n_d	$(3\pm 2)\times 10^{9}$ m^{-3}		Image analysis
r_d iron	$0.5-4$ μm		Microscope[a]
r_d silica	0.5 ± 0.1 μm		Microscope
T_e	2.5 ± 0.2 eV		Double probe (no dust)
E-field	210 ± 20 V/m		Emissive probe (no dust)
B-field	4 mT		Magnetometer
pressure	150 mTorr		Bartron gauge, argon gas
Known			
ρ_{iron}	7860 kg/m^3		Manufacture specifications
ρ_{silica}	2000 kg/m^3		Manufacture specifications
Assumed			
T_n	0.025 eV		Room temperature
T_i	0.025 eV		Room temperature
T_d	$\sim$5 eV		Not measured, estimated
σ_{in}	5×10^{-19} m^{-2}		
σ_{en}	5×10^{-20} m^{-2}		
Computed			
n_e	1.35×10^{13} m^{-3}	$n_e = n_i - Z_d n_d$	Charge neutrality
Z_d	$\sim$2000	$\sim 4\times 10^{8}\ r_d$	Estimated with OML theory
ν_{dn}		$\delta 8\sqrt{2\pi} r_d^2 N V_{nT} m_n/3m_d$	Using $\delta = 1.26$[32]
U_{i0}			

[a] Taken as 0.5 μm.